DroPS 说明文档中文版

黄志琦

huangzhq25@mail.sysu.edu.cn

2025 年 11 月

Contents

1 绪论

1.1 原初功率谱

根据目前标准的宇宙学模型，宇宙微波背景辐射（CMB）和宇宙大尺度结构都源于原初宇宙的微小的，近似服从高斯统计的度规扰动。在线性微扰的层面上，这些原初度规扰动可以被分解为标量、矢量和（二阶）张量。因为矢量扰动会很快衰减，所以我们一般忽略它。宇宙学分析通常引入无量纲、各向同性的标量功率谱 $\mathcal{P}_S(k)$ 和张量功率谱 $\mathcal{P}_T(k)$ 来刻画原初的标量和张量扰动。这里的 k 是共动波矢的大小。

基于慢滚暴胀模型的预言，这两个功率谱通常参数化为幂率形式：

$$\mathcal{P}_S(k) = A_s \left(\frac{k}{k\mathrm{pivot}} \right)^{n_s-1}, \tag{1}$$

和

$$\mathcal{P}_T(k) = r A_s \left(\frac{k}{k\mathrm{pivot}} \right)^{n_t}. \tag{2}$$

现有的 CMB 实验已经对标量功率谱参数 A_s 和 n_s 给出了很强的观测限制 [1]. 在大多数暴胀模型中，张量功率谱的斜率 n_t 都很小，所以在实际数据分析中它或者被近似成零，或者按照单场满滚模型的预言处理（$n_t = -r/8$）. 而剩下的刻画在选定的特征尺度 k_{pivot} 上的张量-标量-比（简称张标比）的参数 r，目前仍然没有观测到它的下限。现在最好的观测上限是 $r < 0.032$（95% 置信度）[2]。虽然这个上限已经排除掉了一些暴胀模型，但是仍然有大量的模型和 $0 < r < 0.032$ 兼容 [3].

1.2 CMB B 模式极化和张标比 r

在 CMB 中探寻原初引力波信号（测量 r）是现代宇宙学的最重要科学目标之一。这项探索聚焦于一个独特的可观测量：B 模式偏振图样。

CMB 光子在其散射早期宇宙中的自由电子时发生了偏振。这个过程在光线上印刻了方向性的偏好，从而产生了两种独特的模式：E 模式（类似于静电荷产生的电场[1]，标量扰动和张量扰动都可以产生）和 B 模式（类似于磁场[2]）。虽然原初等离子体中的密度涨落（标量扰动）能够产生 E 模式，并能通过引力透镜效应产生少量的 B 模式（即所谓的透镜化 B 模式），但它们无法产生原初 B 模式所特有的、大尺度的旋性图样。这正是原初引力波发挥作用之处。理论上产生于暴胀时期的原初引力波在早期宇宙中传播时，会周期性地拉伸和挤压空间，给等离子体施加了一种独特的、旋性的畸变，从而在 CMB 中产生了一种本质上具有旋转特性的偏振模式。

因此，CMB 在大角尺度上的 B 模式功率谱可以作为这些原初引力波的直接示踪物；探测到 CMB 中的大角尺度 B 模式功率谱几乎就等价于测到了原初引力波。因为

---

[1]这仅仅是一个类比。实际上 E 本身是一个标量场；和电场进行类比的极化矢量由 E 的二阶空间导数构造出来

[2]这也仅是类比。实际上 B 是一个赝标量场；和磁场类比的极化矢量由 B 的二阶空间导数构造出来。

$A_s \approx 2.1 \times 10^{-9}$ 几乎是已经被确定的数, (2) 给出的原初引力波的功率谱大小直接正比于参数 r。用 CMB 的大角尺度 B 模式的观测数据限制 r, 就成为窥探极早期物理, 探索引力的量子特性的重要窗口。

1.3 地面小口径 CMB 望远镜

地面小口径的望远镜（SAT）CMB 实验, 包括 BICEP/Keck [4], AliCPT [5, 6, 7], Simons Observatory SATs [8, 9], 以及曾计划的 CMB-S4 SATs [10, 11][3]等, 都有一个共同的目标: 从 CMB 中寻找原初引力波的独有信号。这些望远镜在 (大致在 30–300 GHz 范围内的) 多个频段观测前景相对较弱的部分天区。但即使是这些比较"干净"的天区, 前景依然远强于待测的信号。观测的原始数据将是 CMB 信号, 银河系前景, 大气辐射, 仪器噪声等的叠加。要把微弱的原初引力波信号从数据中提取出来（即测量 r）, 需要十分复杂的成分分离技术。这个文档对应的软件, DroPS (Deriving r from Power Spectra 的缩写), 就是为实现这个目标而设计。

---

[3]目前 CMB-S4 计划已取消。

2 软件使用说明

如果不涉及具体的从时序数据制作天图的流程，而直接从已有的天图出发限制 r，由于分析的是大角尺度（低分辨率）的 CMB 统计，所需要的计算资源并不多[4]。只有在处理真实数据，需要把 DroPS 连接到具体实验对应的天图制作数据管线时，才会涉及大量的计算资源。

因此，为了实现下面的教程的测试例子，用户只需准备一个有几百 GB 硬盘空间的个人电脑。

2.1 安装 DroPS

这个教程是在 Ubuntu 24.04 LTS 系统上测试的，但应该很容易通过微调在其他 linux 系统上实现。如果用户使用的是 Windows 或者 MacOS 系统，很多例子就可能需要较大的改动才能实现——如果环境的调试过于困难，一般的建议是安装一个 Ubuntu 24.04LTS 的子系统。

下面的文档假设用户是在一个 bash 终端（bash terminal）里工作的。

2.1.1 安装系统环境

用 Synaptic Package Manager 或者 "sudo apt install" 安装下面的系统软件包:

- git

- gcc

- gfortran

- cmake

- python3-pip

- python-is-python3

- python3-venv

- openmpi-dev

- libxcb-cursor0

- libcfitsio-dev

- libgsl-dev

---

[4]DroPS 也提供 "天图制作" 的快速模拟器，但是该模拟器仅仅是一种近似，而非是针对某个具体实验的真实时序数据处理。

- libfftw3-dev

- libfftw3-mpi-dev

- libhealpix-dev

2.1.2 建立 Python 虚拟环境

在常用的工作目录（后面用 YourWorkPath 代替）下建立一个 Python 虚拟环境目录：

```
mkdir YourWorkPath/.work
```

（这里的虚拟环境目录名.work 是可以随意选取的，但通常建议以. 开头（默认为隐藏文件夹），以防止日常操作中误删除 Python 包）

然后创立一个 Python 虚拟环境：

```
python -m venv YourWorkPath/.work
```

激活虚拟环境：

```
source YourWorkPath/.work/bin/activate
```

在 Windows 系统里激活虚拟环境可能要在 cmd.exe 里执行

```
YourWorkPath/.work/Scripts/activate.bat
```

或者在 PowerShell 里执行

```
YourWorkPath/.work/Scripts/activate.psl
```

当工作结束时，用

```
deactivate
```

来退出 Python 虚拟环境。

如果你没有其他的 Python 项目，建议把激活虚拟环境的命令放到.bashrc 里

```
echo "source YourWorkPath/.work/bin/activate" >> ${HOME}/.bashrc
```

这样每次启动终端时会自动激活这个虚拟环境。

2.1.3 安装 python 依赖

在激活了上小节安装的 Python 虚拟环境的情况下，我们来安装 DroPS 依赖的 Python 包。

先更新 pip 到最新版以获得 Python 包的正确信息：

```
pip install --upgrade pip
```

进入到工作目录：

```
cd YourWorkPath
```

从 Github 上下载 DroPS 的源码：

```
git clone https://github.com/zqhuang/DroPS
```

然后进入 DroPS 目录

```
cd DroPS
```

用 pip 安装所有依赖包：

```
pip install -r requirements.txt
```

2.1.4 修改 pysm3 包

在上一节安装的依赖包里有一个叫 pysm3 的包，它的功能是模拟前景和 CMB 辐射。我们现在来修改它的源代码来提高模拟效率。虽然修改一个 Python 包的源码一般来说是不被推荐的操作，但是在效率和规范之间反复权衡之后，我们还是采取了这个"权宜之计"来获得更适合 DroPS 的高效模拟功能。在未来如果 pysm3 提供了更为灵活的功能，就可以避免这个不太符合 Python 理念的操作。另外，如果你只准备用 DroPS 的数据分析功能，而不打算使用 DroPS 的天图模拟功能，也可以跳过这小节的操作。

进入 DroPS 目录：

```
cd YourWorkPath/DroPS
```

把 pysm3 安装目录下的文件 models/cmb.py 移动并改名（这是为了备份以保证操作可逆）：

```
mv PATH_TO_pysm3/models/cmb.py cmb_backup.py
```

然后把 DroPS 目录下的 cmb.py 移动到 pysm3 安装目录的 model 文件夹中：

```
cp cmb.py PATH_TO_pysm3/models/
```

这里 PATH_TO_pysm3 代表 pysm3 的安装目录，在 Ubuntu 24.04.3LTS 系统里，你可能会发现这个安装目录是

YourWorkPath/.work/lib/python3.12/site-packages/pysm3

在其他系统环境下，这个安装目录可能有所不同。在 linux 系统下，这个问题比较容易解决：可以先安装 plocate，

```
sudo apt install plocate
```

然后用

```
locate pysm3
```

就可以找到 pysm3 的安装路径。

2.2 参照数据组

在分析（无论是模拟的还是真实观测得到的）观测天图之前，必须模拟一批 CMB、噪音和前景的参照数据组。参照数据组的模拟代表了目前我们对现实（仪器、噪音统计性质、前景统计性质等）的最佳认知。参照数据组可以类比为机器学习中的训练样本[5]。但无论如何，需要注意参照数据组可能和真实数据之间存在系统性的差别。如何尽可能地避免这些可能的差别带来的影响，是 DroPS 一个重要的优化指标。

2.2.1 生成一个时序数据过滤的模拟器

A critical step in processing data from ground-based CMB experiments is the mitigation of ground and atmospheric contamination in the time-ordered data (TOD). Accurately simulating this filtering process necessitates detailed knowledge of the survey strategy, which is often unavailable during the forecasting stage. Fortunately, the overall effect is well-understood: it suppresses large-scale power (low multipoles) in the final maps and introduces non-Gaussian correlations by mixing Fourier modes. For use cases that do not require a precise, survey-specific simulation, DroPS provides a "mock filtering" tool to generate an approximate filtering matrix.

To generate the TOD filtering matrix, run:

---

[5]注意这仅仅是一个类比，DroPS 并不使用深度学习等前沿机器学习技术。

```
python mock_filtering.py
```

and follow the prompts. Enter the healpix resolution (nside, 128 for testing, 256/512 for serious simulations) and the file name for the filtering matrix (e.g. filter_128.pickle). You may also refine the model by entering the parameters ℓ_{cut}, f_{low}, f_{high}, α_{low}, θ_ℓ, θ_m that are defined in Sec. 3.1.

2.2.2 生成参照数据组

Now we are ready to generate the base simulations for given experiments. DroPS comes with four "demo-experiments": Test, AliCPT, SO, and CMBS4. The "Test" demo-experiment is just for testing purpose and does not have a counterpart in reality. The configurations (sky coverage, noise level etc., see Table 1) of the latter three demo-experiments (AliCPT, SO, CMBS4) are similar, but not identical to their counterparts in reality (AliCPT [5], SO-SAT [8] and CMB-S4-SAT [11]). In this documentation we will mainly use the "AliCPT" experiment as examples. We will also use SO for comparison between different foreground modeling and between DroPS and other pipelines in the literature [8].

To begin with, you can simulate noise/cmb/foreground maps for the demo-experiment AliCPT.

```
python simulate.py AliCPT/AliCPT_sim_config.txt
```

Compare the content of configuration file AliCPT/AliCPT_sim_config.txt with Table 1 to understand how the configurations are passed to the script. When no other command-line arguments are passed to simulate.py, it only produces base simulations, that are, a lot of realizations of noise and CMB maps based on the noise model and cosmology that are specified in the configuration file. The foreground maps are only produced once, as we do not yet have a reliable model to describe the "cosmic variance" of foreground emissions. By default, the base simulations use the foreground model ['d0', 's0'] with fixed spectral indices ($\beta_d = 1.54$ for thermal dust, $\beta_s = -3$ for synchrotron). This ['d0', 's0'] foreground map only captures the gross feature of the Galactic emission. The "actual foreground" that we will analyze in the next section can be different from the one used in the base simulations. A robust r measurement pipeline must be insensitive to the finer details of the foreground modeling.

To further understand how the foreground models are defined in pysm3, you may follow its documentation at https://pysm3.readthedocs.io/.

Table 1: Key configurations of DroPS demo-experiments; $\ell_{\rm knee}$ and $\alpha_{\rm knee}$ are defined in Sec. 3.2

	frequency (GHz)	beam FWHM (arcmin)	noise-level $\sigma_{\rm white}$ (μK-arcmin)	$\ell_{\rm knee}$	$\alpha_{\rm knee}$
Test	30	60	1	60	-1.7
($f_{\rm sky} \approx 0.1$)	95	20	1	60	-1.7
	150	20	1	60	-3
	270	10	1	60	-3
AliCPT	27	97	47	30	-2.4
($f_{\rm sky} \approx 0.14$)	40	65	34	30	-2.4
	90	16.2	2.2	50	-2.5
	150	9.7	3.3	50	-3
(+Planck)	217	4.9	50	0^+	-3
SO	27	91	33	15	-2.4
($f_{\rm sky} \approx 0.1$)	39	63	22	15	-2.4
	93	30	2.5	25	-2.5
	145	17	2.8	25	-3
	225	11	5.5	35	-3
	280	9	14	40	-3
CMBS4	30	72.8	2.5	60	-1.7
($f_{\rm sky} \approx 0.1$)	40	72.8	3.15	60	-1.7
	85	25.5	0.622	60	-1.7
	95	22.7	0.552	60	-1.7
	145	25.5	0.87	60	-3
	155	22.7	0.948	60	-3
	220	13	2.46	60	-3
	270	13	4.22	60	-3

2.3 分析天图

In the previous section, we generated a set of base simulations. These serve as a reference library, constructed from a specific noise model, the foreground model ['d0', 's0'], and a set of fiducial r values within a ΛCDM cosmology. Now we can simulate an "observed sky" map. This mock observation uses the same noise model but can employ a different foreground model and, crucially, an r value that is independent of those in the base simulations. DroPS will determine the value of r in this "observed sky" by statistically comparing it against the base simulation library. Conceptually, this "observed sky" is analogous to a "test sample" in machine learning. We may also generate many realizations of the "observed sky" to assess the average offset (bias) between the reconstructed and input r values.

2.3.1 单次模拟天图的分析

Generate the "observed sky" with, e.g.,

```
python simulate.py AliCPT/AliCPT_sim_config.txt maps/AliCPT_ 0.01 999
```

You can replace maps/AliCPT_ with your preferred prefix for the output maps, 0.01 with your preferred fiducial r value, and 999 with your preferred random seed. To test whether DroPS can deal with a spatial variation of the foreground, you may also replace the ['d0', 's0'] foreground model with, e.g., ['d1', 's1'] in the configuration file AliCPT/AliCPT_sim_config.txt.

Now analyze the "observed sky" with

```
python mainpipe.py AliCPT/AliCPT_ana_config.txt maps/AliCPT_
```

Read the configuration file AliCPT/AliCPT_ana_config.txt to understand how to analyze the maps with different settings.

The summary statistics of r and other parameters will be shown on the screen when the analysis is done. More detailed results will be saved in AliCPT/results, a path that is also specified in the configuration file AliCPT/AliCPT_ana_config.txt.

2.3.2 多次模拟天图的分析

In one simulation, the posterior mean value of r can be above or below the input r, and this depends on the random seed. To test whether the r-measurement pipeline is biased or not, we need to apply the pipeline on many simulations with different random seeds.

This time we choose a different foreground model ["d1", "s1"]. Now run the simulations and analyze them by running the following shell script (test_bias.sh in the repository)

```
./test_bias.sh
```

The content of test_bias.sh is shown below.

Listing 1: content of test_bias.sh

```
for i in `seq 100`
do
    python simulate.py AliCPT/AliCPT_sim_config.txt maps/s${i}_  0.01 ${i}  d1s1
    python mainpipe.py AliCPT/AliCPT_ana_config.txt maps/s${i}_ logfile.txt
done
```

Here 0.01 is the fiducial r value; the random seed (bash variable ${i}) runs from 1 to 100; maps/s${i} is the root name (prefix for output files) for each simulation; logfile.txt is the file that saves the reconstructed means and standard deviations of r.

Now plot the saved means and standard deviations of r from logfile.txt, and compare them with the input $r = 0.01$.

```
python utils/plot_rs.py logfile.txt 0.01
```

If the bias of r-measurement is small, the mean of reconstructed mean values of r (dotted blue line) is supposed to be close to the fiducial value (solid orange line), as shown in Figure 1.

2.3.3 真实观测数据的分析

A real experiment comes with its own map making and noise simulation pipelines, and provides base simulations and the actually observed sky maps. To analyze the real data, you can simply replace the base simulations with the maps from the simulation pipeline of the experiment, and replace the realization of sky with the actually observed frequency maps.

2.3.4 和其他分析管线的比较

DroPS has been applied on AliCPT data challenge (simulated 14% sky, 95GHz and 150GHz) and achieved consistent results with other methods [6]. Here we further compare DroPS with three pipelines that have been applied on simulation data of SO-SAT (Wolz
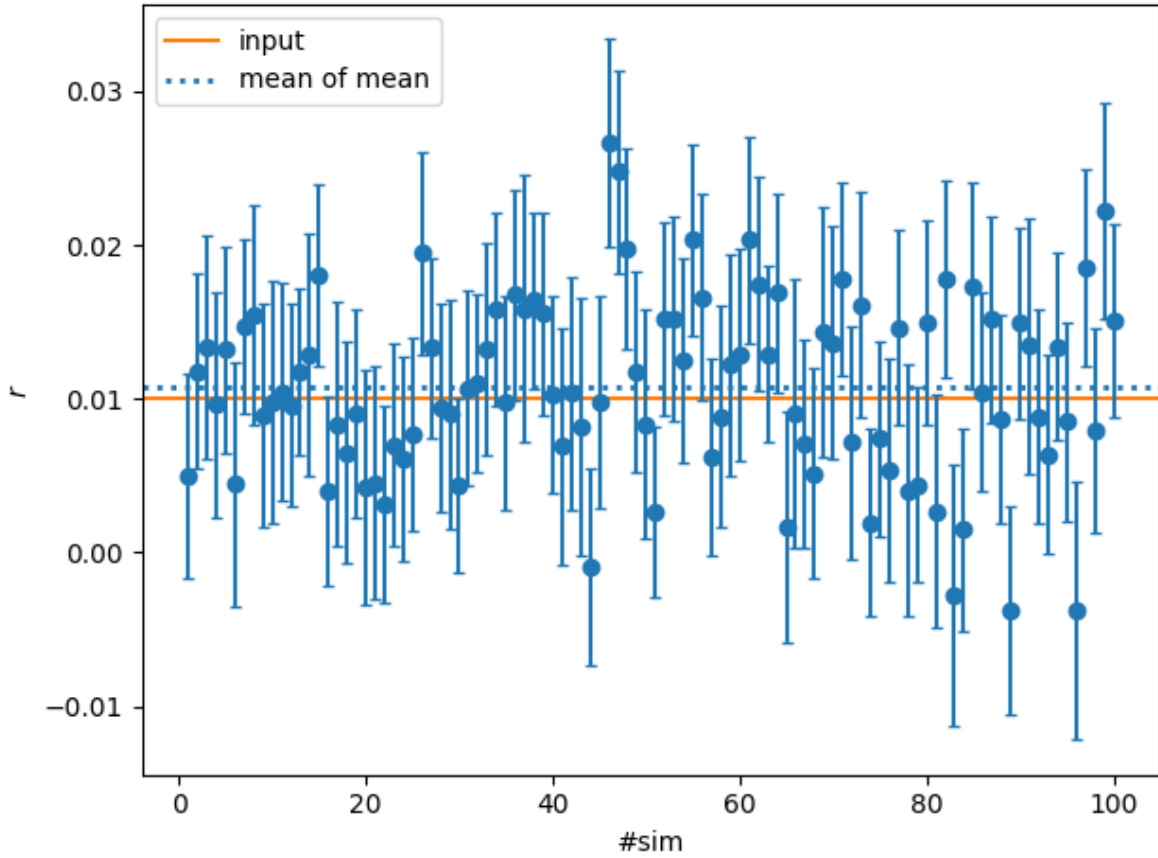
Figure 1: Reconstructed r for 100 realizations of sky with different random seeds. For each sky, the r value is reconstructed by comparing the sky with 300 base simulations. The 100 realizations of sky are simulated with foreground model ['d1','s1'] (spatially varying SED of synchrotron and dust emission), while ['d0', 's0'] (fixed SED) is used in the 300 base simulations.

et al. 2024 [8]). We adopt the optimistic configuration of SO-SAT. The input fiducial r is zero, and in the analyses unphysical negative r is allowed[6]. The results are shown in Figure 2. From top to bottom, foreground models ['d0', 's0'], ['d1', 's1'], and ['dm', 'sm'] are used, respectively[7]. From the left where the reconstructed means of r and the bias (mean of the reconstructed means of r) are shown, we find DroPS has negligible biases for all cases and more stable than the three pipelines tested in Wolz et al. The right column shows σ_r, the statistical uncertainties in r. We again find good consistency between DroPS and the other pipelines.

2.4   天图成分分离

2.4.1   基于似然函数的天图成分分离方法

The most well known method of component separation is probably the internal linear combination (ILC) algorithm and its variations. The basic idea is to isolate a signal - whose frequency dependence is known - by taking linear combination of the frequency maps. To do that in pixel space, the frequency maps have to be smoothed to a common resolution.

For ground-based CMB experiments, however, a key challenge of ILC or ILC-like methods is that TOD filtering and beam convolution are non commutative operations. Consequently, smoothing frequency maps to a common resolution inevitably alters their spectral energy distributions. This inherent limitation explains why, despite its popularity in simulations that neglect TOD filtering effects [8], ILC is often superseded by more computationally intensive, likelihood-based methods in real-world analyses, such as those conducted by BICEP/Keck [12].

DroPS also provides a map-level component separation code. To demonstrate how the code works, we generate a sky realization from the base simulation #0:

```
python utils/combine_sim.py AliCPT/AliCPT_sim_config.txt maps/r3AliCPT0_ 0
```

The above script takes the base simulation #0 and adds the filtered foreground maps, filtered noise maps and filtered CMB maps into sky frequency maps with root name maps/r3AliCPT0_.

Now we do component separation

---

[6]in DroPS this is realized by setting r_lowerbound negative in the configuration file

[7]The model ['dm', 'sm'] does not come with pysm3 and needs to be prepared by the user. See [8] for its definition.
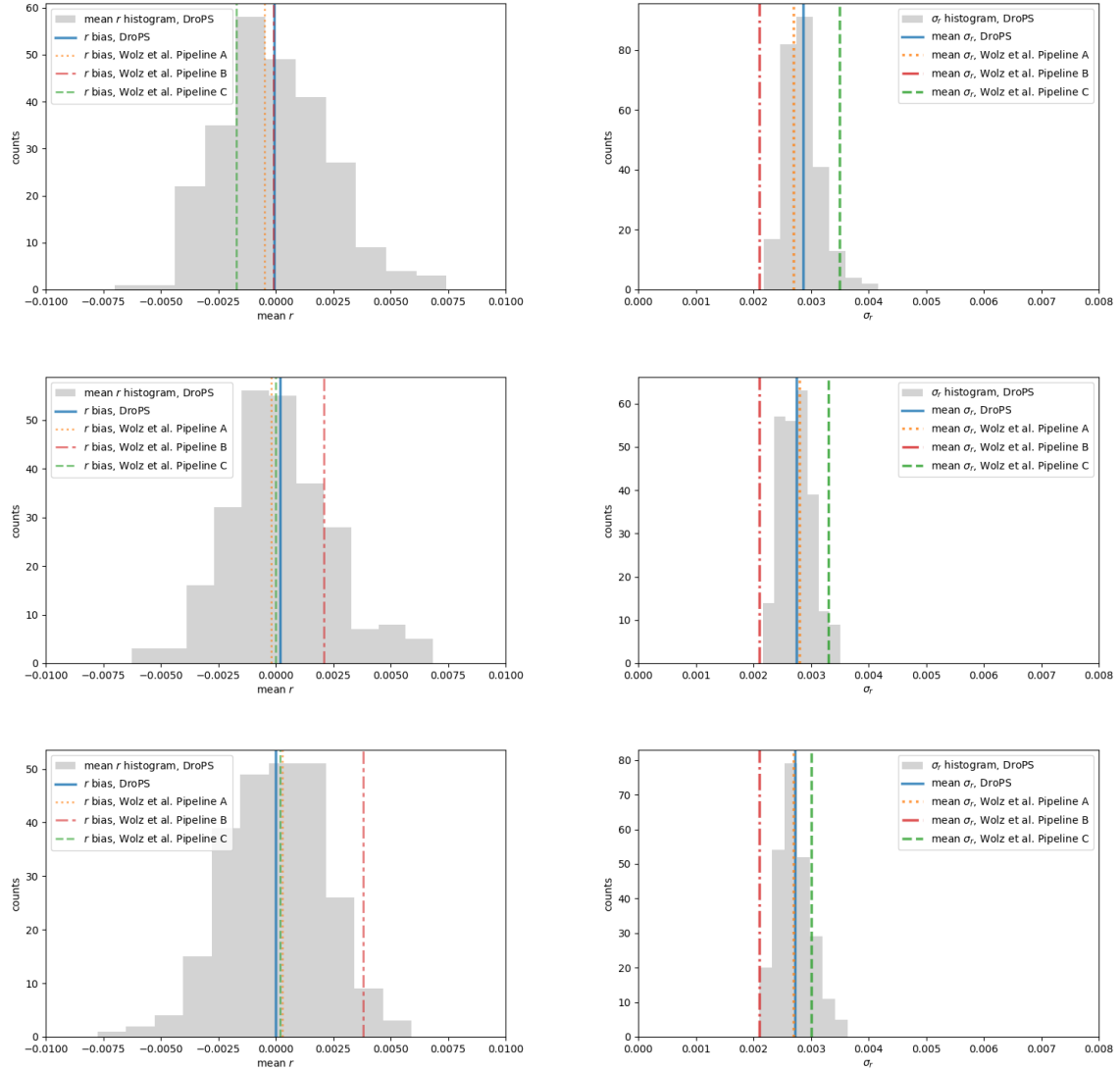
Figure 2: Comparing DroPS with three pipelines that are described in Wolf et al. [8]. From top to bottom, foreground models ['d0', 's0'], ['d', 's1'], and ['dm', 'sm'] are used, respectively. Left and right columns are the distribution of reconstructed mean r and σ_r, respectively.

```
python compsep.py AliCPT/AliCPT_sim_config.txt maps/r3AliCPT0_
```

The code uses Stochastic Gradient Langevin Dynamics (SGLD) method to search the maximum of the likelihood described in Sec. 3.6. It typically takes a few days to run compsep.py for the first time, on a personal computer. When the gradient templates are built, the code runs much faster, typically takes only a few hours on a personal computer. Typically you need to run it multiple times to obtain a well converged CMB B-mode map. Figure 3 shows the result for the maps simulated with AliCPT/AliCPT_sim_config.txt. The E maps are recovered very well. While significant residual noises remain in the B maps.

For real data analyses, the calculation of gradient template involves map making and therefore takes even longer time to built. Fortunately, the gradient template can be built in a parallel way. The template can be built for $\ell \in [\ell_{\min}, \ell_{\max}]$ by running

```
python compsep.py AliCPT/AliCPT_sim_config.txt maps/r3AliCPT0_ lmin lmax
```

Thus, with parallel I/O that is commonly supported in modern architectures, the task can be decomposed into many sub-tasks with different lmin and lmax. You need ∼100GB disk space to store all the gradient templates.

2.4.2 可视化

DroPS provides a few tools to display the maps on the screen.

The script utils/viewfits.py displays the fits maps.

```
python utils/viewfits.py NHmask_G_128.fits
```

If you have a map example_IQU.fits with stokes I, Q, U components, you can run

```
python utils/viewfits.py example_IQU.fits mapind
```

with mapind = 0, 1, 2 for I, Q, U components, respectively.

DroPS often saves partial-sky maps in npy format. Now suppose the mask file is mask.fits. To display these masked-sky maps, use utils/viewnpy.py:

```
python utils/viewnpy.py mask.fits example_IQU.npy mapind
```

with mapind = 0, 1, 2 for I, Q, U components, respectively.

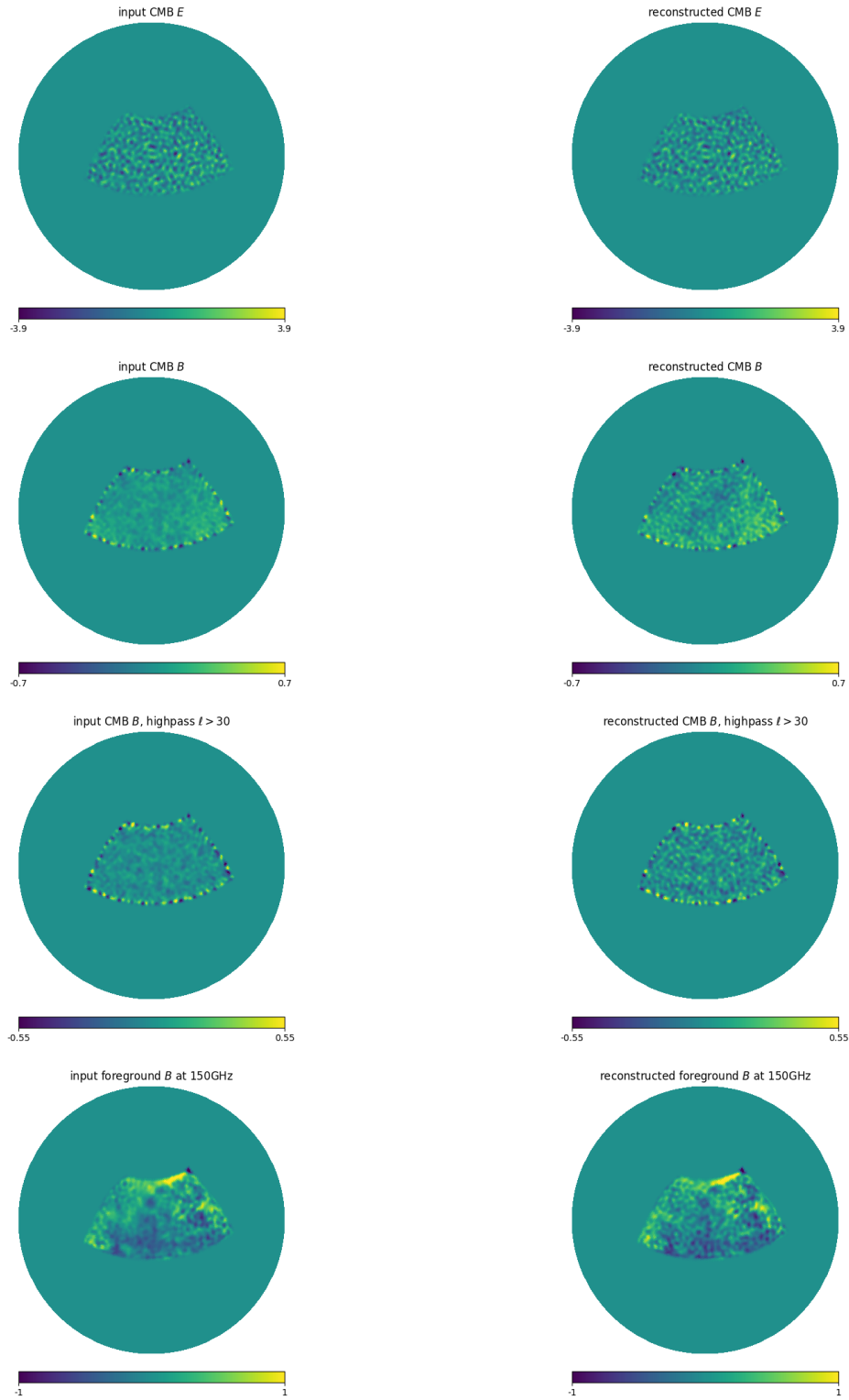To display E/B components, use utils/viewEB.py:

Figure 3: Component separation for maps simulated with AliCPT/AliCPT_sim_config.txt. All maps are smoothed with top-hat low-pass filter at $\ell \leq 160$.

```
python utils/viewEB.py mask.fits example_IQU.npy E/B
```

3 软件技术细节

In this section I assume the reader has cosmological background and is familiar with Healpix [13].

DroPS analyzes the power spectrum by dividing the multipole range into a few bins and computing the band powers[8] for masked maps using NaMaster [14]. For measuring the tensor-to-scalar ratio r, the analysis typically focuses on the range $20 \lesssim \ell \lesssim 200$ with a small number of bins. A resolution of nside = 256 is sufficient for this purpose, while nside = 128 may be adequate for quick estimates. However, caution is advised when performing operations such as changing the map resolution or rotating to a different coordinate system, as these can introduce significant E-to-B leakage in low-resolution maps. For any analysis involving these manipulations, we recommend using a higher resolution of nside = 512.

The data vector for the likelihood analysis consists of the band powers derived from the filtered sky maps. These are constructed as follows: band powers between different frequency channels are computed directly as cross-power spectra, while for a single channel, they are obtained from the cross-power of pairs of independent season maps within that channel. This design ensures that the expectation value of the noise band power is zero in all cases, which effectively eliminates bias from imperfect noise modeling. This approach represents a standard in modern CMB analysis.

Let n_{bin} be the number of ℓ-bins, n_ν the number of frequency channels, and n_{fld} the number of fields (e.g., TT, TE, EE, BB). The data vector comprises the band powers $D_\ell^{XY}(\nu_1, \nu_2)$, indexed by:

- Multipole bin centered at ℓ;

- Field XY;

- All ranked frequency pairs (ν_1, ν_2) with $\nu_1 \leq \nu_2$.

As noted previously, for $\nu_1 = \nu_2$, the band power is computed by averaging over season-map cross-spectra. The total number of ranked frequency pairs is $n_\nu(n_\nu + 1)/2$, making the full data vector length $N_d = \frac{1}{2} n_{\mathrm{fld}} n_{\mathrm{bin}} n_\nu(n_\nu + 1)$. For r-measurement with limited computing or storage resources, we recommend using only the BB spectra ($n_{\mathrm{fld}} = 1$), as they contain nearly all the information on r.

The fundamental approach is to evaluate the likelihood of the observed data vector $D_\ell^{XY}(\nu_1, \nu_2)$ (abstractly written as D^{obs}) given a model prediction (abstractly written as

---

[8]A band power represents the average power spectrum within a given ℓ bin.

D^{model}). Taking a Gaussian approximation, the likelihood is:

$$\mathcal{L} = \frac{1}{(2\pi)^{N_d/2}\sqrt{\det}} \exp\left[-\frac{1}{2}(\mathbf{D}^{\text{obs}} - \mathbf{D}^{\text{model}})^{T\ -1}(\mathbf{D}^{\text{obs}} - \mathbf{D}^{\text{model}})\right], \qquad (3)$$

The model is constructed from the signal components:

$$\mathbf{D}^{\text{model}} = \mathbf{D}^{\text{CMB}} + \mathbf{D}^{\text{fg}}, \qquad (4)$$

where D^{CMB} and D^{fg} are the expected band powers from the CMB and foregrounds. The noise expectation is zero due to the exclusive use of cross-correlations. The total covariance Cov encompasses all variance from noise, foregrounds, and CMB.

Prior to discussing the specific noise, CMB, and foreground models or the technical estimation of Cov, we will outline two key components: the map-making simulators for the base simulations, and how the TOD filtering is modeled throughout the pipeline.

3.1 时序数据过滤和天图制作

A critical preprocessing step in ground-based CMB experiments is the TOD filtering, which isolates the faint CMB signal from dominant, structured ground noise. Observations from the ground are heavily contaminated by low-frequency noise from atmospheric emission and instrumental $1/f$ noise. TOD filtering operates in the time domain to identify and subtract these systematic contaminants, which often exhibit characteristic temporal or scan-synchronous patterns distinct from the CMB. By applying high-pass or more sophisticated modal filters, it suppresses large-scale noise while aiming to preserve the intrinsic CMB signal, enabling the production of high-fidelity sky maps.

Although a linear process, TOD filtering is equivalent to applying a dense matrix that is difficult to model without detailed knowledge of the experiment's scanning strategy. Consequently, DroPS does not include full map-making pipelines for specific experiments. Instead, it provides streamlined "map-making" simulators. These simulators approximate the net effect of the pipeline by combining a few linear operations in both pixel and harmonic space, guided by the survey mask and a handful of parameters that capture the essential features of TOD filtering.

Specifically, the simulator applies the following operations to an input map:

1. Generate a filtering matrix (in harmonic space) with six parameters ℓ_{cut}, f_{low}, f_{high}, α, θ_ℓ and θ_m. Specifically, the matrix is given by

$$M_{\ell'm',\ell m} = \begin{cases} \sqrt{[1 - 2(\theta_\ell + \theta_m)]\,F_\ell}, & \text{if } \ell' = \ell, m' = m; \\ \sqrt{F_\ell\theta_\ell}G_{\text{random}} & \text{if } |\ell' - \ell| = 1, m' = m \\ \sqrt{F_\ell\theta_m}G_{\text{random}} & \text{if } \ell' = \ell, |m' - m| = 1 \\ 0, & \text{else} \end{cases}$$

where

$$F_\ell \equiv f_{\mathrm{high}} \left\{ 1 - f_{\mathrm{low}} \exp\left[-\left(\frac{\ell}{\ell_{\mathrm{cut}}} \right)^\alpha \right] \right\}$$

and G_{random} is a random Gaussian number. For each matrix element G_{random} is drawn independently.

2. Generate a smoothed mask by apodizing the mask edges using a C2-type kernel with an apodization scale of 2 degrees [15].

3. PMultiply the input map pixel-wise by the smoothed mask.

4. Perform a spherical harmonic transform to obtain harmonic coefficients $a_{\ell m}$.

5. Apply the filtering matrix

$$a_{\ell' m'} = \sum_{\ell,m} M_{\ell' m', \ell m} a_{\ell m}.$$

6. Perform an inverse spherical harmonic transform back to a map.

7. Multiply the resulting map pixel-wise by the original (unapodized) mask.

When

```
python mock_filtering
```

is called. It generates a pickle file that saves the random numbers (G_{random}) in operation 1.

When simulating maps, the pickle file is specified in the configuration file (e.g. AliCPT/AliCPT_sim_config.txt). DroPS loads the pickle file and performs "map making" (seven linear operations in sequence, as specified above).

The "map-making" simulator is designed for computational efficiency, requiring far fewer resources than a full pipeline that processes actual time-ordered data. It is a simplified model whose purpose is not to replicate every detail, but to capture the dominant large-scale effects of TOD filtering—namely, power suppression and mode mixing—for simulation-based studies.

In the analysis stage, DroPS operates without prior knowledge of the specific TOD filtering applied in the simulations. It phenomenologically models the net filtering effect using a coupling matrix $F_{\ell \ell'}$. This matrix is structured such that its main diagonal captures the power suppression in each multipole bin, while the first off-diagonals capture the mode coupling between adjacent bins; all other elements are set to zero. By default, this matrix is calibrated empirically by performing a least-squares fit that compares the band powers of filtered versus unfiltered noise maps from the base simulations.

An important caveat is that while TOD filtering is a linear operation on the map, its effect on the power spectrum is not strictly linear. The band-diagonal coupling matrix $F_{\ell\ell'}$ is therefore a simplified model. Consequently, the design of DroPS intentionally minimizes reliance on this approximate model to ensure robustness. (See Sec. 3.3 for more details.)

3.2 噪音模型

DroPS adopts a noise model for its temperature power spectrum following the established approach in Refs. [16, 8]:

$$N_\ell = N_{\text{white}} \left[1 + \left(\frac{\ell}{\ell_{\text{knee}}} \right)^{\alpha_{\text{knee}}} \right]. \tag{5}$$

Here, the $1/f$ noise component is parameterized by the knee multipole ℓ_{knee} and the slope α_{knee}. The white noise level N_{white} is derived from the configuration parameter σ_{white} (see Table 1) as

$$N_{\text{white}} = \sigma_{\text{white}}^2, \tag{6}$$

where σ_{white} must be in units of μK-radian[9].

For the demo-experiments, the polarization noise spectra are simplified to $N_\ell^{EE} = N_\ell^{BB} = 2N_\ell^{TT}$. While this relation is not exact for real instruments, it provides a reasonable approximation in many cases.

It is important to note that the analytic model in Eq. (5) is used exclusively for generating the base simulations. During the data analysis stage, DroPS bypasses this model and computes the noise covariance directly from the base simulations themselves. Furthermore, the expectation value of the noise power spectrum is always zero in the analysis because DroPS exclusively employs cross-power spectra between different frequency channels or observation seasons, thereby inherently deriving noise-debiased power spectra.

3.3 CMB 模型

3.3.1 宇宙学

DroPS assumes standard Lambda cold dark matter (ΛCDM) with an additional parameter r. For the demo experiments, the default cosmological parameters for base simulations are listed in Table 2.

Unlike the noise statistics, which can be empirically derived from the base simulations, the CMB statistics depend on underlying cosmological parameters—most notably the unknown tensor-to-scalar ratio rr. This fundamental difference necessitates a more

---

[9]To convert from μK-arcmin, multiply by a factor of $\frac{\pi}{10800}$.

Table 2: Default cosmological parameters for base simulations

parameter	definition	default value
$\Omega_b h^2$	baryon density	0.02242
$\Omega_c h^2$	cold dark matter density	0.11933
θ_{MC}	angular extension of sound horizon	0.0104101
τ_{re}	reionization optical depth	0.0561
$\ln(10^{10} A_s)$	logarithm amplitude of primordial scalar power	3.047
n_s	spectral index of primordial scalar power	0.9665
r	tensor-to-scalar ratio	$r_0 = 0$ or $r_1 = 0.03$

sophisticated approach for modeling the CMB band powers and their contribution to the signal covariance matrix.

3.3.2 去透镜化

Gravitational lensing by large-scale structure distorts the primordial CMB, smoothing its acoustic peaks and converting a portion of the E-mode polarization into a secondary B-mode signal. This lensing-induced B-mode acts as a dominant foreground on small scales, obscuring the fainter primordial B-modes from inflationary gravitational waves. While the expectation value of this lensing B-mode power can be theoretically predicted and subtracted, the actual lensing potential in our observed Universe randomly fluctuates around this mean—a source of cosmic variance. For measurements targeting an uncertainty of $\sigma_r \lesssim 10^{-3}$, this unpredictable fluctuation becomes a significant contaminant.

Delensing addresses this by statistically reconstructing the actual lensing distortion from high-resolution CMB data or external tracers and removing its specific imprint from the observed maps. This process cleans the cosmic foreground, sharpens the CMB's original features, and suppresses the confounding lensing B-mode power, thereby dramatically enhancing the sensitivity to primordial signals.

In DroPS, the implementation assumes that an ideal lensing potential map is available from external sources. While such a map would, in principle, allow for complete delensing, practical limitations prevent perfect removal. To model this, DroPS introduces a delensing efficiency parameter $\epsilon_{\mathrm{delens}}$ (delens_fac in the configuration file), which specifies the fraction of the lensing effect to be removed. Concretely, the process is performed by rescaling the input lensing potential map by a factor of $(1 - \epsilon_{\mathrm{delens}})$ before applying the delensing operation.

3.3.3 宇宙学参数限制

The primary goal of DroPS is to infer the tensor-to-scalar ratio rr, which is by default the only free cosmological parameter. Users can choose to vary the full set of standard $\Lambda\Lambda$CDM parameters by setting vary_cosmology = True in the configuration file. However, since the large-scale polarization data from ground-base SATs alone provide weak constraints on the background cosmology, DroPS applies a Gaussian prior based on Planck+BAO results [1] to ensure the parameters remain within physically reasonable ranges[10].

The base simulations are generated with two fiducial values of the tensor-to-scalar ratio: $r = 0$ and $r = r_1 > 0$. By averaging over these simulations, we obtain the expected CMB band powers, $\langle D_\ell^{\text{CMB}}(r = 0)\rangle$ and $\langle D_\ell^{\text{CMB}}(r = r_1)\rangle$. The recommended value for r_1 is 0.03 (approximately the current 90% confidence level upper limit), which is user-configurable.

Under the standard cosmological model, and assuming other parameters θ are fixed to their fiducial values θ_{fid}, the CMB band powers exhibit an approximately linear response to rr. DroPS leverages this by modeling the CMB band powers as a linear interpolation between the two simulated benchmarks, which inherently includes all instrumental effects:

$$D_\ell^{\text{CMB}} = (1 - w)\langle D_\ell^{\text{CMB}}(r = 0)\rangle + w\langle D_\ell^{\text{CMB}}(r = r_1)\rangle + \Delta_{\text{correction}}. \tag{7}$$

The interpolation weight w is defined as $w \equiv \max\left[\min\left(\frac{r}{r_1}, 1\right), -1\right]$, effectively clamping the interpolation for $|r| > r_1$.

The correction term $\Delta_{\text{correction}}$ applies the TOD filtering matrix $F_{\ell\ell'}$ only to the deviation from this fiducial interpolated spectrum:

$$\Delta_{\text{correction}} = \sum_{\ell'} F_{\ell\ell'} \left[D_{\ell'}^{\text{CMB}}(r, \theta) - (1 - w)D_{\ell'}^{\text{CMB}}(r = 0, \theta_{\text{fid}}) - wD_{\ell'}^{\text{CMB}}(r = r_1, \theta_{\text{fid}}) \right],$$
$$\tag{8}$$

This design is highly efficient for the most likely scenario in next-generation experiments, where $|r| < r_1$ and cosmological parameters are well-constrained. In this case, the term inside the brackets is small, and the filtering matrix—whose model might be approximate—is applied only to a residual, thereby minimizing the impact of any inaccuracies in the filtering model on the final result.

---

[10]This prior can be disabled by modifying mainpipe.py, but doing so may lead to poor convergence in the Monte Carlo sampling or numerical instability.

3.4 前景模型

3.4.1 尘埃热辐射和同步辐射的基本模型

The primary diffuse foregrounds in CMB polarization—Galactic thermal dust and synchrotron radiation—possess spectral energy distributions (SEDs) that are distinctly different from the CMB's blackbody spectrum. This spectral distinction is the basis for component separation, which necessitates a minimum of three frequency channels to disentangle the CMB, dust, and synchrotron signals.

The frequency dependence of dust temperature fluctuation is modeled as a modified black-body (MBB) spectrum, which converted to the CMB μK unit is

$$W_d(\nu; \nu_{\rm ref}, \beta_d) = \left(\frac{\nu}{\nu_{\rm ref}}\right)^{\beta_d-1} e^{\frac{h(\nu_{\rm ref}-\nu)}{k_B T_{\rm CMB}}} \left(\frac{e^{\frac{h\nu}{k_B T_{\rm CMB}}}-1}{e^{\frac{h\nu_{\rm ref}}{k_B T_{\rm CMB}}}-1}\right)^2 \left(\frac{e^{\frac{h\nu_{\rm ref}}{k_B T_{\rm MBB}}}-1}{e^{\frac{h\nu}{k_B T_{\rm MBB}}}-1}\right), \qquad (9)$$

where $T_{\rm MBB} \approx 20\,{\rm K}$ is the effective temperature of MBB spectrum, $T_{\rm CMB} \approx 2.726\,{\rm K}$ is the CMB temperature, β_d is the frequency spectral index, and $\nu_{\rm ref}$ is an arbitrarily chosen reference frequency. Because thermal dust emission dominates the high-frequency bands, we often choose a high reference frequency, e.g., $\nu_{\rm ref,dust} \sim 300\,{\rm GHz}$.

The frequency dependence of synchrotron temperature fluctuation is modeled as a power-law spectrum, which converted to the CMB μK unit is

$$W_s(\nu; \nu_{\rm ref}, \beta_s) = \left(\frac{\nu}{\nu_{\rm ref}}\right)^{\beta_s-2} e^{\frac{h(\nu_{\rm ref}-\nu)}{k_B T_{\rm CMB}}} \left(\frac{e^{\frac{h\nu}{k_B T_{\rm CMB}}}-1}{e^{\frac{h\nu_{\rm ref}}{k_B T_{\rm CMB}}}-1}\right)^2, \qquad (10)$$

where β_s is the frequency spectral index, and $\nu_{\rm ref}$ is an arbitrarily chosen reference frequency. Because thermal synchrotron radiation dominates the low-frequency bands, we often choose a low reference frequency, e.g., $\nu_{\rm ref,sync} \sim 30\,{\rm GHz}$.

When there is no risk of confusion, we may write $W_d(\nu; \nu_{\rm ref}, \beta_d)$ as $W_d(\nu)$, and $W_s(\nu; \nu_{\rm ref}, \beta_d)$ as $W_s(\nu)$. When β_d (β_s) is known, we can convert a dust (synchrotron) map at frequency ν_1 to map at frequency ν_2 with a scaling factor $\frac{W_d(\nu_2)}{W_d(\nu_1)}$ ($\frac{W_s(\nu_2)}{W_{s,2}}$). (Note that this ratio does not depend on the choice of reference frequency.) Finally, for a frequency band with (normalized) frequency distribution $f(\nu)$, $W_d(\nu)$ should be replaced with averaged weight $\int W_d(\nu) f(\nu)\, {\rm d}\nu$.

By default DroPS treats the band powers of *filtered* dust and synchrotron maps as free parameters. The advantage of doing so is two folds. First, we do not need to worry about the accuracy of $F_{\ell\ell'}$ modeling, as we are directly modeling the band powers of filtered maps. Second, although the average dust/synchrotron power spectra is likely to be smooth, their power spectra in a small sky area may have random "cosmic variance", which is taken into account in the free-bandpower parametrization. The disadvantage of abandoning the smoothness assumption on foreground band powers is that it degrades the

constraining power on r. However, this extra uncertainty is physical, as it correctly reflects that the foreground band powers in a small patch of sky can have random fluctuations around a smooth model.

A blind parametrization of the dust-dust, dust-synchrotron, and synchrotron-synchrotron band powers involves $3n_{\mathrm{fld}}n_{\mathrm{bin}} + 2$ independent parameters. Here $+2$ corresponds to β_d and β_s. Even in the case where only $XY = BB$ is used, the number of foreground parameters is typically $\gtrsim 20$. This poses some challenge to the convergence of Monte Carlo Markov Chain (MCMC) simulations, which is used in DroPS for parameter inference. However, when the data contain a high-frequency channel and a low-frequency channel, which respectively give good "initial guesses" of the dust and synchrotron band powers, we empirically find the MCMC runs can reach good convergence.

If the number of available frequency channel is small or the noise is large (target $\sigma_r \gtrsim 0.01$), however, smooth parametrization of foreground power is recommended. The reason is that the "cosmic variance" of foreground becomes a tiny effect compared to noise and filter modeling uncertainty. The smooth model of foreground band powers - which is modeled as a quadratic function of ℓ - can be turned on in the configuration file by setting analytic_fg = True.

3.4.2 前景能谱的空间变化: 矩展开方法

The above discussion is based on the assumption of constant β_d and β_s. For experiments that covers a significant portion of the sky, however, it is unlikely that β_d (β_s) will be strictly a constant across a large area of the sky [17] . DroPS deals with the spatial variation of foreground spectral indices with moment expansion approximation [18] or Taylor expansion methods, which can be switched on by setting freq_decorr_model="ME" or freq_decorr_model="Taylor" in the configuration file. Set freq_decorr_model=None if strictly constant β_d and β_s are wanted. By default, DroPS uses the moment expansion method, details of which are given below.

We take thermal dust emission B-mode map for example. At frequency ν, the map is

$$B(\nu, \mathbf{n}) = W_d(\nu; \nu_{\mathrm{ref}}, \beta_d)B(\nu_{\mathrm{ref}}, \mathbf{n}), \tag{11}$$

if there were no spatial variation of β_d. Here $\mathbf{n}$ is the map pixel vector, and $B(\nu_{\mathrm{ref}}, \mathbf{n})$ is the map at reference frequency (reference map). Now consider small spatial variation $\delta\beta_d(\mathbf{n})$ and expand to second order of $\delta\beta_d(\mathbf{n})$

$$B(\nu, \mathbf{n}) = \left\{ W_d(\nu; \nu_{\mathrm{ref}}, \beta_d) + \frac{\partial W_d}{\partial \beta_d}\delta\beta_d(\mathbf{n}) + \frac{1}{2}\frac{\partial^2 W_d}{\partial \beta_d^2}\left[\delta\beta_d(\mathbf{n})\right]^2 \right\} B(\nu_{\mathrm{ref}}, \mathbf{n}). \tag{12}$$

Since $W_d \propto \left(\frac{\nu}{\nu_{\mathrm{ref}}}\right)^{\beta_d}$, Eq. (12) can be explicitly written as

$$B(\nu, \mathbf{n}) = W_d(\nu; \nu_{\mathrm{ref}}, \beta_d) \left\{ 1 + \delta\beta_d(\mathbf{n}) \ln \frac{\nu}{\nu_{\mathrm{ref}}} + \frac{1}{2} \left[\delta\beta_d(\mathbf{n}) \ln \frac{\nu}{\nu_{\mathrm{ref}}} \right]^2 \right\} B(\nu_{\mathrm{ref}}, \mathbf{n}). \qquad (13)$$

We first consider the full-sky case and do spherical harmonic transform. Assuming $\delta\beta_d(\mathbf{n}) = \sum \beta_{\ell m} Y_{\ell m}(\mathbf{n})$ and $B(\nu, \mathbf{n}) = \sum a_{\ell m}(\nu) Y_{\ell m}(\mathbf{n})$.

$$
\begin{aligned}
a_{\ell m}(\nu) &= W_d(\nu; \nu_{\mathrm{ref}}, \beta_d) \int Y_{\ell m}^*(\mathbf{n}) \left\{ 1 + \delta\beta_d(\mathbf{n}) \ln \frac{\nu}{\nu_{\mathrm{ref}}} + \frac{1}{2} \left[\delta\beta_d(\mathbf{n}) \ln \frac{\nu}{\nu_{\mathrm{ref}}} \right]^2 \right\} B(\nu_{\mathrm{ref}}, \mathbf{n}) \, \mathrm{d}^2\mathbf{n} \\
&= W_d(\nu; \nu_{\mathrm{ref}}, \beta_d) \left[a_{\ell m}^{\mathrm{ref}} + \ln \frac{\nu}{\nu_{\mathrm{ref}}} g_{\ell m}^{\mathrm{ref}} + \left(\ln \frac{\nu}{\nu_{\mathrm{ref}}} \right)^2 h_{\ell m}^{\mathrm{ref}} \right] \qquad (14)
\end{aligned}
$$

where

$$a_{\ell m}^{\mathrm{ref}} = a_{\ell m}(\nu_{\mathrm{ref}}), \qquad (15)$$

$$g_{\ell m}^{\mathrm{ref}} = (-1)^m \sqrt{\frac{2\ell+1}{4\pi}} \sum_{\ell_1, m_1, \ell_2, m_2} a_{\ell_1, m_1}^{\mathrm{ref}} \beta_{\ell_2, m_2} \sqrt{(2\ell_1+1)(2\ell_2+1)} \begin{pmatrix} \ell_1 & \ell_2 & \ell \\ 0 & 0 & 0 \end{pmatrix} \begin{pmatrix} \ell_1 & \ell_2 & \ell \\ m_1 & m_2 & -m \end{pmatrix}, \qquad (16)$$

and

$$
\begin{aligned}
h_{\ell m}^{\mathrm{ref}} &= (-1)^m \frac{\sqrt{2\ell+1}}{8\pi} \sum_{\ell_1, m_1, \ell_2, m_2, \ell_3 m_3} a_{\ell_1, m_1}^{\mathrm{ref}} \beta_{\ell_2, m_2} \beta_{\ell_3, m_3} \sqrt{(2\ell_1+1)(2\ell_2+1)(2\ell_3+1)} \\
&\quad \times \sum_{\ell_4, m_4} (-1)^{m_4} (2\ell_4+1) \begin{pmatrix} \ell_2 & \ell_3 & \ell_4 \\ m_2 & m_3 & -m_4 \end{pmatrix} \begin{pmatrix} \ell_2 & \ell_3 & \ell_4 \\ 0 & 0 & 0 \end{pmatrix} \begin{pmatrix} \ell_4 & \ell_1 & \ell \\ 0 & 0 & 0 \end{pmatrix} \begin{pmatrix} \ell_4 & \ell_1 & \ell \\ m_4 & m_1 & -m \end{pmatrix}. \qquad (17)
\end{aligned}
$$

Assuming $\delta\beta_d(\mathbf{n})$ is a random Gaussian field that is uncorrelated with the reference map $B(\nu_{\mathrm{ref}}, \mathbf{n})$ and keeping only up to second order of $\delta\beta_d$, we have

$$\langle (a_{\ell m}^{\mathrm{ref}})^* g_{\ell m}^{\mathrm{ref}} \rangle = 0, \qquad (18)$$

$$\langle (h_{\ell m}^{\mathrm{ref}})^* g_{\ell m}^{\mathrm{ref}} \rangle = 0, \qquad (19)$$

and

$$\langle (h_{\ell m}^{\mathrm{ref}})^* h_{\ell m}^{\mathrm{ref}} \rangle = 0. \qquad (20)$$

Here $\langle \cdot \rangle$ represents cosmic expectation value.

Further approximately treating $B(\nu_{\mathrm{ref}}, \mathbf{n})$ a random Gaussian field, we may also use the power spectra $C_\ell^{\mathrm{ref}} \equiv \langle (a_{\ell m}^{\mathrm{ref}})^* a_{\ell m}^{\mathrm{ref}} \rangle$ and $S_\ell \equiv \langle (\beta_{\ell m})^* \beta_{\ell m} \rangle$ to express some non-zero expectation values. Specifically, they are

$$\langle (g_{\ell m}^{\mathrm{ref}})^* g_{\ell m}^{\mathrm{ref}} \rangle = \frac{1}{4\pi} \sum_{\ell_1, \ell_2} C_{\ell_1}^{\mathrm{ref}} S_{\ell_2} (2\ell_1+1)(2\ell_2+1) \begin{pmatrix} \ell_1 & \ell_2 & \ell \\ 0 & 0 & 0 \end{pmatrix}^2, \qquad (21)$$

and

$$\langle (a^{\text{ref}}_{\ell m})^* h^{\text{ref}}_{\ell m} \rangle = \frac{1}{8\pi} C^{\text{ref}}_\ell \sum_{\ell_2} (2\ell_2 + 1) S_{\ell_2}. \tag{22}$$

To derive Eq. (21), we have used the identity

$$\sum_{m_1,m_2} \begin{pmatrix} \ell_1 & \ell_2 & \ell_3 \\ m_1 & m_2 & m_3 \end{pmatrix} \begin{pmatrix} \ell_1 & \ell_2 & \ell'_3 \\ m_1 & m_2 & m'_3 \end{pmatrix} = \begin{cases} \frac{1}{2\ell_3+1}, & \text{if } |\ell_1 - \ell_2| \leq \ell_3 \leq \ell_1 + \ell_2,\ \ell_3 = \ell'_3,\ m_3 = m'_3 \\ 0, & \text{otherwise} \end{cases}, \tag{23}$$

namely the orthogonal property of 3-j symbol. To derive Eq. (22), we have used the identity

$$\sum_m (-1)^{\ell-m} \begin{pmatrix} \ell & \ell & n \\ m & -m & 0 \end{pmatrix} = \begin{cases} \sqrt{2\ell+1}, & \text{if } n = 0 \\ 0, & \text{else} \end{cases}. \tag{24}$$

The power spectrum between two frequency maps $B(\nu, \mathbf{n})$ and $B(\nu', \mathbf{n})$ is then

$$
\begin{aligned}
C_\ell(\nu, \nu') &= \langle a_{\ell m}(\nu) a_{\ell m}(\nu') \rangle \\
&= W_d(\nu; \nu_{\text{ref}}, \beta_d) W_d(\nu'; \nu_{\text{ref}}, \beta_d) \\
&\quad \times \left\{ C^{\text{ref}}_\ell + \langle (g^{\text{ref}}_{\ell m})^* g^{\text{ref}}_{\ell m} \rangle \ln \frac{\nu}{\nu_{\text{ref}}} \ln \frac{\nu'}{\nu_{\text{ref}}} + \langle (a^{\text{ref}}_{\ell m})^* h^{\text{ref}}_{\ell m} \rangle \left[\left(\ln \frac{\nu}{\nu_{\text{ref}}} \right)^2 + \left(\ln \frac{\nu'}{\nu_{\text{ref}}} \right)^2 \right] \right\}. \\
&= W_d(\nu; \nu_{\text{ref}}, \beta_d) W_d(\nu'; \nu_{\text{ref}}, \beta_d) \\
&\quad \times \left\{ C^{\text{ref}}_\ell \left[1 + \frac{1}{8\pi} \left(\ln^2 \frac{\nu}{\nu_{\text{ref}}} + \ln^2 \frac{\nu'}{\nu_{\text{ref}}} \right) \sum_{\ell_2} (2\ell_2 + 1) S_{\ell_2} \right] \right. \\
&\quad \left. + \frac{1}{4\pi} \ln \frac{\nu}{\nu_{\text{ref}}} \ln \frac{\nu'}{\nu_{\text{ref}}} \sum_{\ell_1,\ell_2} C^{\text{ref}}_{\ell_1} S_{\ell_2} (2\ell_1 + 1)(2\ell_2 + 1) \begin{pmatrix} \ell_1 & \ell_2 & \ell \\ 0 & 0 & 0 \end{pmatrix}^2 \right\}, \tag{25}
\end{aligned}
$$

The above result can be written in a more compact way

$$C_\ell(\nu, \nu') = W_d(\nu) W_d(\nu') \left\{ C^{\text{ref}}_\ell \left[1 + \mu \left(\ln^2 \frac{\nu}{\nu_{\text{ref}}} + \ln^2 \frac{\nu'}{\nu_{\text{ref}}} \right) \right] + \varepsilon_\ell \ln \frac{\nu}{\nu_{\text{ref}}} \ln \frac{\nu'}{\nu_{\text{ref}}} \right\}, \tag{26}$$

where

$$\mu \equiv \frac{1}{8\pi} \sum_{\ell_2} (2\ell_2 + 1) S_{\ell_2} \tag{27}$$

is proportional to the variance of $\delta\beta_d$, and

$$\varepsilon_\ell \equiv \frac{1}{4\pi} \sum_{\ell_1,\ell_2} C^{\text{ref}}_{\ell_1} S_{\ell_2} (2\ell_1 + 1)(2\ell_2 + 1) \begin{pmatrix} \ell_1 & \ell_2 & \ell \\ 0 & 0 & 0 \end{pmatrix}^2 \tag{28}$$

is proportional to the convolution between β_d and the reference map.

The minimal parametrization then involve two unknown spectra C^{ref}_ℓ and S_ℓ, while μ is a derived parameter that relies on S_ℓ.

In general we deal with maps in a masked fractional sky. If the variance of $\delta\beta_d$ is dominated by small-scale fluctuations, we may still use Eqs. (26) as an approximation and

replace S_{ℓ_2} with $S_{\ell_2} f_{\text{fsky}}$ in Eq. (27) and Eq. (28), where f_{sky} is the sky fraction. However, this approximation may not work very well, for the following reasons.

1. Large-scale variation of β_d has been observed [17], while small-scale variation of β_d remains a conjecture. Therefore, it is possible that the variance of $\delta\beta_d$ may be dominated by large-scale modes, whose information is partially missing in a masked sky.

2. Similarly, because for masked sky we are dealing with band powers with limited scale coverage, we cannot accurately evaluate the convolution ε_ℓ.

3. The mask and non-Gaussianity of the dust map may induce coupling between different modes. This will lead to extra scale-dependent contribution to μ and ε_ℓ.

The net effect is then the relation between μ, C_ℓ^{ref} (in form of band powers) and S_ℓ (also in form of band powers) becomes vague in the masked-sky case, and μ essentially becomes scale-dependent if mode mixing is not negligible. The final model of band powers used in DroPS is then

$$D_\ell(\nu,\nu') = W_d(\nu)W_d(\nu') \left\{ D_\ell^{\text{ref}} \left[1 + \mu_\ell \left(\ln^2 \frac{\nu}{\nu_{\text{ref}}} + \ln^2 \frac{\nu'}{\nu_{\text{ref}}} \right) \right] + \varepsilon_\ell \ln \frac{\nu}{\nu_{\text{ref}}} \ln \frac{\nu'}{\nu_{\text{ref}}} \right\}, \quad (29)$$

where D_ℓ^{ref}, μ_ℓ and ε_ℓ (both in form of band powers) are directly taken as independent parameters. To avoid overfitting and consistently keep the μ_ℓ and ϵ_ℓ terms perturbative, we assume an upperbound for $|\mu_\ell|$ and $|\epsilon_\ell|$ (default: 0.05).

At the time of writing, there is no observational confirmation or rejection of spatial variation of β_d on small scales. Eqs. (27,28) imply that ε_ℓ and μ_ℓ are positive parameters, if the extra contribution from mode mixing is negligible. However, applying this physical prior can bias the r measurement if there is actually no spatial variation of β_d, and we have no clue whether the mode mixing can be safely neglected. Therefore, by default DroPS does not apply the positiveness prior. If wanted, the positiveness prior which can be turned on by setting ME_is_positive = True in the configuration file.

The treatment of synchrotron is exactly the same, as the dependence of W_d on β_d and W_s on β_s is identical ($W_d \propto (\nu/\nu_{\text{ref}})^{\beta_d}$ and $W_s \propto (\nu/\nu_{\text{ref}})^{\beta_s}$).

In summary, we have generalized the moment expansion method to masked sky, but still have ignored many complexities that may emerge in reality, such as possible correlation between $\delta\beta_d$, $\delta\beta_s$ and the reference map. Although some of the complexities may be absorbed into the free parameters μ_ℓ and ε_ℓ, we do not expect Eq. (29) covers all possible degrees of freedom. Nevertheless, at least for small perturbations around the base (constant-SED) model, moment expansion method is a good tool to account for the foreground complexity.

3.4.3   前景频率去相关: 泰勒展开方法

For the base (constant-SED) model of dust (synchrotron), the band powers satisfy $[D_\ell(\nu,\nu')]^2 = D_\ell(\nu,\nu)D_\ell(\nu',\nu')$. Complexity of foreground such as spatial variation of SED in general weakens the correlation between different frequency maps, that is,

$$[D_\ell(\nu,\nu')]^2 \leq D_\ell(\nu,\nu)D_\ell(\nu',\nu'), \tag{30}$$

with equality if and only if $\nu = \nu'$.

Note that, however, the moment expansion formula Eq. (29) (or the full-sky version Eq. (26)) does not explicitly follow this physically motivated inequality. Motivated by the inequality (30), DroPS provides a phenomenological model, which can be turned on by setting fg_decorr_model = "Taylor" in the configuration file. The idea of this model is to Taylor expand the spectral index β_d in the ν, ℓ space. Specifically, the band powers of dust in is parameterized as

$$D_\ell(\nu,\nu') = W_d(\nu;\nu_{\text{ref}}, \beta_d + \delta\beta_{d,\ell} + \gamma_d\frac{\nu}{\nu_{\text{ref}}})W_d(\nu';\nu_{\text{ref}}, \beta_d + \delta\beta_{d,\ell} + \gamma_d\frac{\nu'}{\nu_{\text{ref}}}) \exp\left[-\frac{\ln^2\frac{\nu}{\nu'}}{Q_\ell}\right]D_\ell^{\text{ref}}, \tag{31}$$

where β_d and γ_d are the average SED and the frequency running of SED; D_ℓ^{ref} is the reference band power; $\delta\beta_{d,\ell}$ describes the variation of β_d in ℓ space; $Q_\ell > 0$ describes the logarithm spacing of frequency decorrelation. (Frequency decorrelation is significant if $\ln\frac{\nu}{\nu'} \gtrsim Q_\ell$.)

The moment expansion and Taylor expansion methods typically induce shifts of r on the order of a few $\times 10^{-4}$. We use the more precise demo-experiment SO to highlight the impact of foreground modeling. Figure 4 compares the reconstructed r using the base model (constant SED), the moment expansion, and the Taylor expansion methods. Each data point and error bar represent the mean and standard deviation, respectively, averaged over 250 random realizations of the "observed sky." Our analysis shows that the moment expansion method remains nearly unbiased across all tested scenarios, albeit at the cost of a modest increase in uncertainty. The Taylor expansion method also performs robustly in the presence of foreground frequency decorrelation. However, in the absence of such decorrelation, it tends to systematically underestimate the value of r.

3.5   带功率的相关矩阵

While the covariance matrix of the band powers could, in principle, be estimated directly from simulations, this approach faces a practical challenge: the covariance matrix typically contains over a thousand free elements, which cannot be robustly constrained by the few hundred simulations typically available. To overcome this, DroPS implements
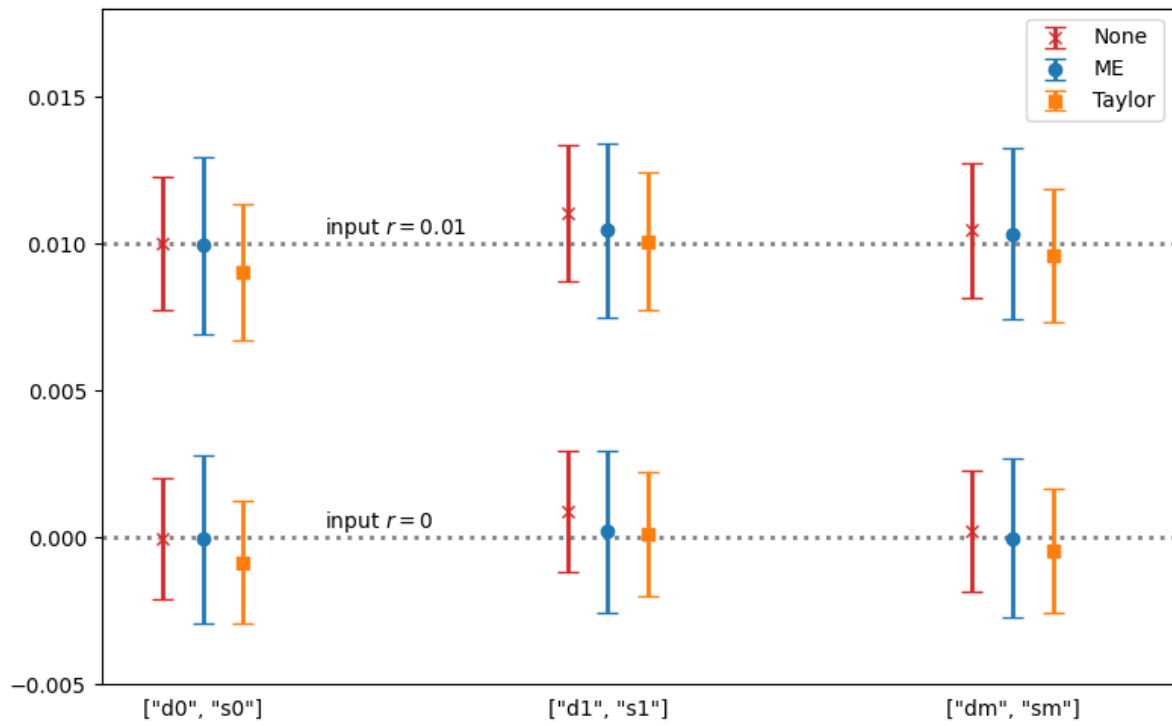
Figure 4: Comparison between base model (None), moment expansion method (ME) and Taylor expansion method(Taylor). Simulations are obtained with SO/SO_sim_config.txt.

a two-step stabilization procedure: it applies "noise cleaning" by neglecting noise correlations across different channels or observation seasons, and enforces "scale separation" by ignoring correlations between widely separated multipole bins.

DroPS decomposes the covariance matrix into three components: the noise covariance, the signal covariance, and the signal×noise covariance. The advantage of doing so is that noise covariance can be "cleaned" with the prior knowledge that noise in different frequency channels (or observation seasons) are uncorrelated. DroPS also assumes that the noise T, E, B are mutually uncorrelated[11]. Consequently, the noise covariance between $D_\ell^{XY}(\nu_1, \nu_2)$ and $D_{\ell'}^{X'Y'}(\nu_1', \nu_2')$ is nonzero only if $XY = X'Y'$ and $(\nu_1, \nu_2) = (\nu_1', \nu_2')$. This substantially reduces the degrees of freedom and improves the accuracy of noise covariance estimation.

By default, DroPS assumes no correlation between different multipole bins (ell_cross_range = 0 in the configuration file). Optionally, it can model correlations between adjacent (ell_cross_range = 1) or next-to-adjacent bins (ell_cross_range = 2). However, simply truncating the covariance matrix to these limited off-diagonal blocks can violate its positive-definite property, introducing unphysical "ghost modes" with negative eigenvalues that lead to catastrophic overfitting. To balance information retention with numerical stability, DroPS applies suppression factors to the off-diagonal ℓ blocks. The optimal factors, listed in Table 3, are derived analytically for a small number of bins or numerically for a larger set. Specifically:

- For ell_cross_range = 1, the first off-diagonal blocks are multiplied by a factor f_1.

- For ell_cross_range = 2, the first and second off-diagonal blocks are multiplied by factors f_1 and f_2, respectively.

Empirical tests show that the correlations between adjacent ℓ bins and next-to-adjacent ℓ bins usually do not have a significant impact on the constraint on r and foreground parameters. Figure 5 shows an example. The simulation is done with AliCPT/AliCPT_sim_config.txt with fiducial $r = 0.01$ and random seed 5; the analyses are done with AliCPT/AliCPT_ana_config.txt (with ell_cross_range = 0, 1, 2 respectively). The input fiducial $r = 0.01$ and $\beta_d = 1.54$ are marked with lightgray dotted lines in the figure. The contours are plotted with the script utils/plot_cont.py that comes with DroPS.

The signal and signal×noise covariance matrices are cosmology-dependent. DroPS pre-computes them at the two fiducial points, $r = 0$ and $r = r_1$, from the base simulations. Within the interval $0 < r < r_1$, the covariances are interpolated according to their known scaling with r: the signal covariance scales with r^2 and is thus interpolated linearly

---

[11]In the default settings where BB band powers are used, this assumption is not used.

Table 3: suppression factors (f_1 for adjacent and f_2 for next-to-adjacent bins)

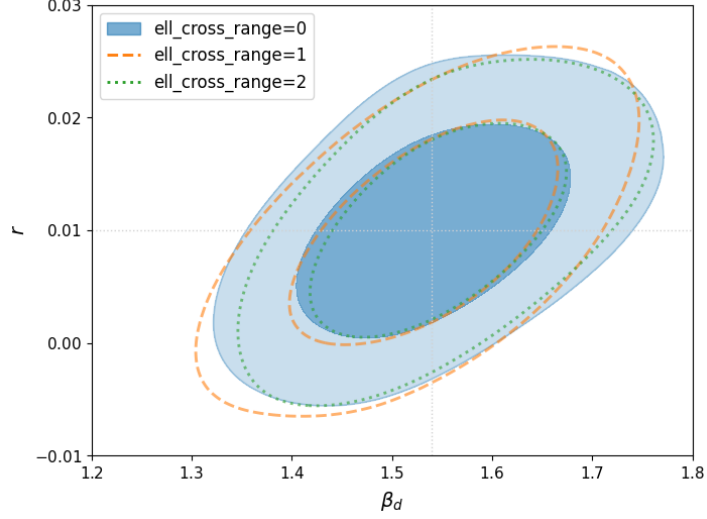|	ell_cross_range = 1	ell_cross_range = 2
# ℓ bins	f_1	f_1, f_2
2	1	-
3	$\frac{1}{\sqrt{2}}$	1, 1
4	$\frac{\sqrt{5}-1}{2}$	$\frac{\sqrt{3}}{2}, \frac{1}{2}$
5	$\frac{1}{\sqrt{3}}$	$\sqrt{2 - \sqrt{\frac{28}{3}}\cos\frac{\pi+\arccos\sqrt{\frac{27}{28}}}{3}}, \sqrt{\sqrt{\frac{28}{3}}\cos\frac{\pi+\arccos\sqrt{\frac{27}{28}}}{3} - 1}$
6	$\frac{2}{3} - \frac{\sqrt{28}}{3}\cos\frac{\pi+\arccos\frac{1}{\sqrt{28}}}{3}$	$\sqrt{\frac{3}{2} - \frac{4\sqrt{7}}{9}\cos\frac{\pi-\arccos\frac{17}{7\sqrt{7}}}{3} + \frac{7}{9}\cos\frac{2\pi-2\arccos\frac{17}{7\sqrt{7}}}{3}},$ $\frac{5}{6} - \frac{\sqrt{7}}{3}\cos\frac{\pi-\arccos\frac{17}{7\sqrt{7}}}{3}$
7	$\frac{\sqrt{2-\sqrt{2}}}{2}$	0.74222720 , 0.25777280
8	0.53208889	0.74535599 , $\frac{1}{3}$
9	0.52573111	0.73967857 , 0.29430138
10	0.52110856	0.73205081 , 0.26794919
11	0.51763809	0.72458926 , 0.24925315
12	0.51496392	0.72430917 , 0.29789426
13	0.51285843	0.72360680 , 0.27639320
14	0.51117030	0.72095982 , 0.25989153
15	0.50979558	0.71754959 , 0.24694521
16	0.50866092	0.71688142 , 0.28311858
17	0.50771331	0.71707895 , 0.26835006
18	0.50691364	0.71592096 , 0.25627141
19	0.50623256	0.71404546 , 0.24626867
20	0.50564767	0.71340854 , 0.27515189
∞	$\frac{1}{2}$	$\frac{1}{\sqrt{2}}, \frac{1}{4}$

Figure 5: Impact of the correlations between adjacent ℓ bins and next-to-adjacent ℓ bins

in r^2, while the signal×noise covariance scales with r and is interpolated linearly in r. For values $|r| > r_1$, DroPS uses the covariance evaluated at $r = r_1$, deliberately avoiding any extrapolation to prevent the introduction of unphysical modes and catastrophic overfitting.

3.6 天图成分分离的似然函数

For map-level component separation, the likelihood $\mathcal{L} \propto e^{-\chi^2/2}$ is constructed under a Gaussian noise model, where

$$\chi^2 = v_{\mathrm{noise}}^T N^{-1} v_{\mathrm{noise}}, \tag{32}$$

Here, v_{noise} represents the noise frequency maps, and N is their covariance matrix. In pixel space, the dimension of v_{noise} is $n_{\mathrm{pix}} n_\nu$, which for experiments like AliCPT or SO-SAT with $\gtrsim 10\%$ sky coverage typically exceeds 10^4. This makes the covariance matrix N, with 10^8 elements, prohibitively large to estimate robustly from simulations and to invert efficiently.

To overcome this, the BICEP/Keck analysis [12] adopts a diagonal approximation of N in pixel space, considering only pixel auto-correlations. DroPS employs a more accurate approximation by assuming N is diagonal in harmonic space. This approach better captures the correlations inherent in the data while remaining computationally tractable.

We label a pixel with index j ($j = 1, 2, \ldots, n_{\mathrm{pix}}$), and frequency channels with index k ($k = 1, 2, \ldots, n_\nu$). The CMB maps are identical in all frequency channels, and are

modeled as

$$(Q \pm iU)_{\text{CMB,j,k}} = -\sum_{\ell=0}^{\ell_{\max}} \sum_{m=-\ell}^{\ell} (c_{\ell m}^E \pm ic_{\ell m}^B) \,_{\pm 2}Y_{\ell m}(\mathbf{n}_j), \tag{33}$$

where $\mathbf{n}_j$ is the directional vector of the j-th pixel. The expansion bases $_{\pm 2}Y_{\ell m}$ are spin-weighted spherical harmonics. Note that here $c_{\ell m}^E$ and $c_{\ell m}^B$ are harmonic coefficients of the full-sky CMB map. Degeneracy between these parameters are expected for partial sky observations.

Due to limited frequency resolution, BICEP/Keck analysis models the foreground maps (v_{FG}) as a single component (thermal dust). DroPS takes a more accurate two-component model with emission from Galactic synchrotron and thermal dust. The dust maps are modeled as

$$(Q \pm iU)_{\text{dust,j,k}} = -\int W_d(\nu) f_k(\nu) \, \mathrm{d}\nu \sum_{\ell=0}^{\ell_{\max}} \sum_{m=-\ell}^{\ell} (d_{\ell m}^E \pm id_{\ell m}^B) \,_{\pm 2}Y_{\ell m}(\mathbf{n}_j), \tag{34}$$

where the frequency dependence function W_d is defined in Eq. (9) and $f_k(\nu)$ is the frequency distribution of the k-th frequency channel. Synchrotron maps are modeled similarly,

$$(Q \pm iU)_{\text{sync,j,k}} = -\int W_s(\nu) f_k(\nu) \, \mathrm{d}\nu \sum_{\ell=0}^{\ell_{\max}} \sum_{m=-\ell}^{\ell} (s_{\ell m}^E \pm is_{\ell m}^B) \,_{\pm 2}Y_{\ell m}(\mathbf{n}_j), \tag{35}$$

where W_s is given in Eq. (10).

The sky model $(Q + iU)_{\text{sky}}$ is the sum of Eqs. (33, 34, 35). Passing the sky model through the TOD filtering and map making process, we obtain the filtered sky maps. Subtracting the filtered sky maps from the observed (filtered) maps, we obtain filtered noise maps in pixel space. To compute the likelihood, we decompose the noise maps into harmonic space,

$$M_j(Q \pm iU)_{\text{noise,filtered,j,k}} = -\sum_{\ell=0}^{\ell_{\max}} \sum_{m=-\ell}^{\ell} (\tilde{n}_{\ell m}^E \pm i\tilde{n}_{\ell m}^B) \,_{\pm 2}Y_{\ell m}(\mathbf{n}_j). \tag{36}$$

Here M_j is pixel value of a smoothed mask, whose edges are apodized using a C2-type kernel with an apodization scale of 2 degrees [15]. The purpose of introducing such a smoothed mask is to suppress unphysical modes due to sharp-edge and to reduce E-to-B leakage.

On the other hand, we can calculate $\tilde{n}_{\ell m}^E$ and $\tilde{n}_{\ell m}^B$ from the filtered noise maps in the base simulations, and compute their diagonal covariance $\tilde{N}_{\ell m}^E \equiv \langle |\tilde{n}_{\ell m}^E|^2 \rangle$ and $\tilde{N}_{\ell m}^B \equiv \langle |\tilde{n}_{\ell m}^B|^2 \rangle$. For most mask shapes, the m-dependencies of $\tilde{N}_{\ell m}^E \equiv \langle |\tilde{n}_{\ell m}^E|^2 \rangle$ and $\tilde{N}_{\ell m}^B \equiv \langle |\tilde{n}_{\ell m}^E|^2 \rangle$ are very weak, and mostly reflect the statistic fluctuations due to finite sampling. Therefore, DroPS uses the m-averaged pseudo power spectra $\tilde{N}_\ell^E$ and $\tilde{N}_\ell^B$ to construct

the likelihood in harmonic space. The likelihood $\propto e^{-\chi^2/2}$ is given by

$$\chi^2 = f_{\text{sky}} \sum_{\ell=0}^{\ell_{\text{max}}} \sum_{m=-\ell}^{\ell} \frac{|\tilde{n}_{\ell m}|^2}{N_\ell}. \tag{37}$$

References

[1] Nabila Aghanim, Yashar Akrami, Mark Ashdown, et al. Planck 2018 results-vi. cosmological parameters. *Astronomy & Astrophysics*, 641:A6, September 2020.

[2] M. Tristram, A. J. Banday, K. M. Górski, R. Keskitalo, C. R. Lawrence, K. J. Andersen, R. B. Barreiro, J. Borrill, L. P. L. Colombo, H. K. Eriksen, R. Fernandez-Cobos, T. S. Kisner, E. Martínez-González, B. Partridge, D. Scott, T. L. Svalheim, and I. K. Wehus. Improved limits on the tensor-to-scalar ratio using BICEP and Planck data. *Physical Review D*, 105(8):083524, April 2022.

[3] John Ellis and David Wands. Inflation (2023). *arXiv e-prints*, page arXiv:2312.13238, December 2023.

[4] P. A. R. Ade, Z. Ahmed, M. Amiri, et al. BICEP/Keck XV: The BICEP3 Cosmic Microwave Background Polarimeter and the First Three-year Data Set. *Astrophysical Journal*, 927(1):77, March 2022.

[5] Hong Li, Si-Yu Li, Yang Liu, Yong-Ping Li, and Xinmin Zhang. Tibet's window on primordial gravitational waves. *Nature Astronomy*, 2:104–106, February 2018.

[6] Junzhou Zhang, Shamik Ghosh, Jiazheng Dou, Yang Liu, Siyu Li, Jiming Chen, Jiaxin Wang, Zhaoxuan Zhang, Jacques Delabrouille, Mathieu Remazeilles, Chang Feng, Bin Hu, Hao Liu, Larissa Santos, Pengjie Zhang, Wen Zhao, Le Zhang, Zhi-Qi Huang, Hong Li, and Xinmin Zhang. Forecast of Foreground Cleaning Strategies for AliCPT-1. *Astrophysical Journal Supplement Series*, 274(2):26, October 2024.

[7] Yang Liu, Lei Ming, Marco Drewes, and Hong Li. AliCPT Sensitivity to Cosmic Reheating. *arXiv e-prints*, page arXiv:2503.21207, March 2025.

[8] Kevin Wolz, Susanna Azzoni, Carlos Hervías-Caimapo, Josquin Errard, Nicoletta Krachmalnicoff, David Alonso, Carlo Baccigalupi, Antón Baleato Lizancos, Michael L. Brown, Erminia Calabrese, Jens Chluba, Jo Dunkley, Giulio Fabbian, Nicholas Galitzki, Baptiste Jost, Magdy Morshed, and Federico Nati. The Simons Observatory: Pipeline comparison and validation for large-scale B-modes. *Astronomy & Astrophysics*, 686:A16, June 2024.

[9] Emilie Hertig, Kevin Wolz, Toshiya Namikawa, et al. The Simons Observatory: Combining cross-spectral foreground cleaning with multitracer B-mode delensing for improved constraints on inflation. *Physical Review D*, 110(4):043532, August 2024.

[10] Kevork Abazajian, Graeme E. Addison, Peter Adshead, et al. CMB-S4: Forecasting Constraints on Primordial Gravitational Waves. volume 926, page 54, February 2022.

[11] Sebastian Belkner, Julien Carron, Louis Legrand, Caterina Umiltà, Clem Pryke, Colin Bischoff, and CMB-S4 Collaboration. CMB-S4: Iterative Internal Delensing and r Constraints. *Astrophysical Journal*, 964(2):148, April 2024.

[12] BICEP/Keck Collaboration, P. A. R. Ade, Z. Ahmed, M. Amiri, D. Barkats, R. Basu Thakur, et al. BICEP/Keck XX: Component-separated maps of polarized CMB and thermal dust emission using Planck and BICEP/Keck Observations through the 2018 Observing Season. *arXiv e-prints*, page arXiv:2509.21648, September 2025.

[13] K. M. Górski, E. Hivon, A. J. Banday, B. D. Wandelt, F. K. Hansen, M. Reinecke, and M. Bartelmann. HEALPix: A Framework for High-Resolution Discretization and Fast Analysis of Data Distributed on the Sphere. *Astrophysical Journal*, 622(2):759–771, April 2005.

[14] David Alonso, Javier Sanchez, Anže Slosar, and LSST Dark Energy Science Collaboration. A unified pseudo-C_ℓ framework. *MNRAS*, 484(3):4127–4151, April 2019.

[15] J. Grain, M. Tristram, and R. Stompor. Polarized CMB power spectrum estimation using the pure pseudo-cross-spectrum approach. *Physical Review D*, 79(12):123515, June 2009.

[16] Peter Ade, James Aguirre, Zeeshan Ahmed, et al. The Simons Observatory: science goals and forecasts. *JCAP*, 2019(2):056, February 2019.

[17] P. A. R. Ade, M. Amiri, S. J. Benton, et al. Analysis of Polarized Dust Emission Using Data from the First Flight of SPIDER. *Astrophysical Journal*, 978(2):130, January 2025.

[18] S. Azzoni, M. H. Abitbol, D. Alonso, A. Gough, N. Katayama, and T. Matsumura. A minimal power-spectrum-based moment expansion for CMB B-mode searches. *JCAP*, 05:047, 2021.